Volume 11
Number 12
28 March 2023
Pages 3893–4256

Journal of Materials Chemistry C

Materials for optical, magnetic and electronic devices

rsc.li/materials-c

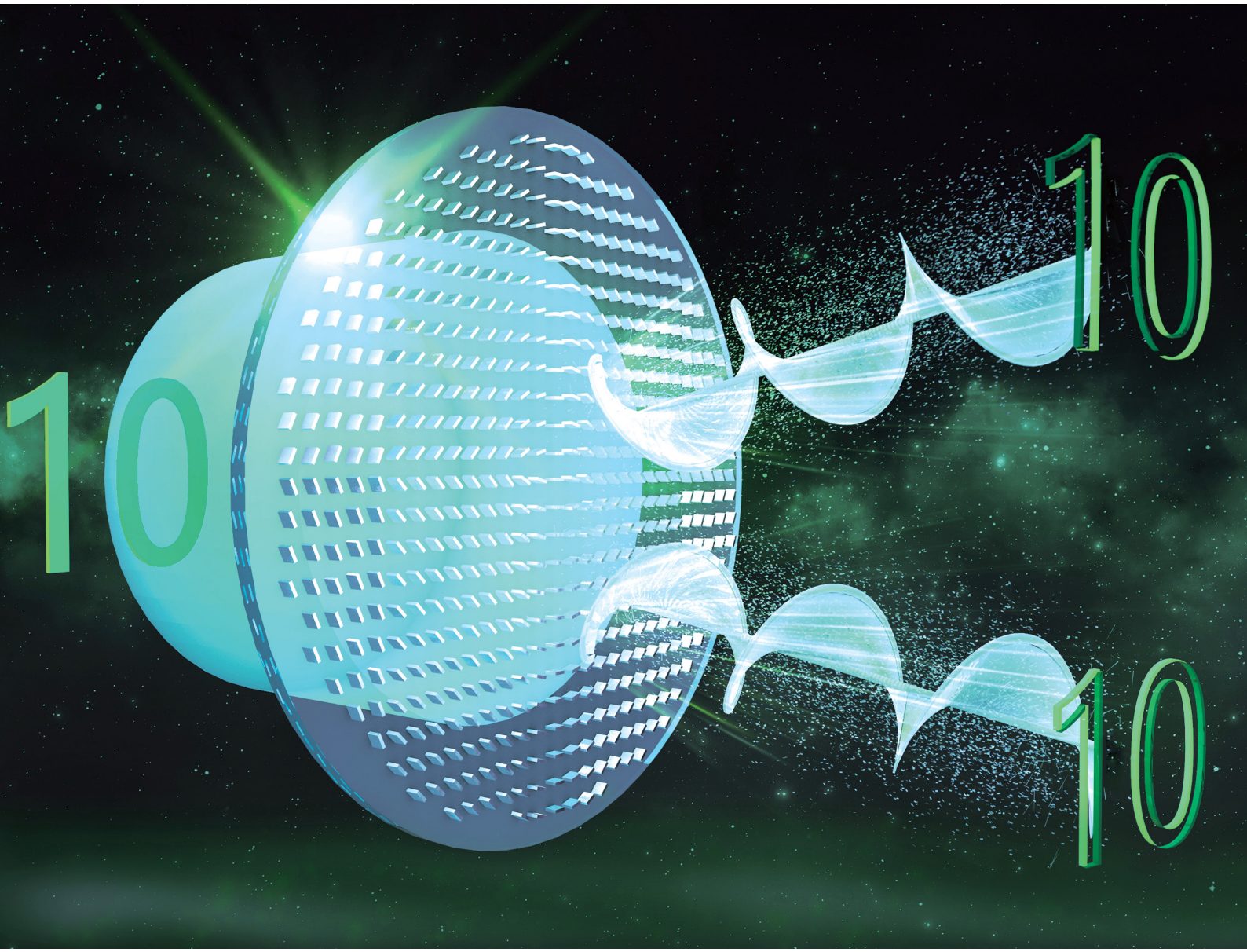

ISSN 2050-7526

ROYAL SOCIETY OF CHEMISTRY

PAPER

Yao Hu *et al.*

Computing metasurface capable of broad-band switchable anisotropic edge-enhanced imaging

10 YEARS ANNIVERSARY

Journal of Materials Chemistry C

ROYAL SOCIETY OF CHEMISTRY

PAPER

View Article Online
View Journal | View Issue

Cite this: J. Mater. Chem. C, 2023, 11, 3956

Computing metasurface capable of broad-band switchable anisotropic edge-enhanced imaging†

Qun Hao,[a] Wenli Wang,[a] Jing Wang,[b] Qianhui Li,[a] Yao Hu,*[a] Shaohui Zhang[a] and Liandong Yu[b]

Received 9th January 2023,
Accepted 28th February 2023

DOI: 10.1039/d3tc00092c

rsc.li/materials-c

Anisotropic edge enhancement imaging along different directions possesses the capability to extract different morphological information from an object which plays a vital role in weak edge detection in imaging. Building a simple, miniature, switchable anisotropic edge enhancement imaging device is extremely absorbing. Here, we design a 2D material, *i.e.*, a helicity-multiplexing dielectric metasurface for anisotropic edge-enhanced imaging. More importantly, this 2D material is prioritized to satisfy two sets of unrelated phase profiles, relying on different helicities of the incident beam. It can function as two different anisotropic edge enhancement filters along different directions by incorporating the 4f imaging system and dynamically switching its function by altering the helicity of the incident beam. Furthermore, a hybrid imaging device based on this 2D material can work across a visible broadband spectrum, which is potentially applicable in biomedical imaging and optical analog computing.

Introduction

Fast and reliable anisotropic edge detection and image processing are vital capabilities required in biomedical imaging[1,2] and outdoor infrared detection.[3] Many digital domain computations using integrated circuits have been proposed for enhancing imaging detection at the expense of high-power consumption and low speed.[4,5] Optical analog computing can overcome these limits because it modulates the field of the incident beam by placing appropriate optical elements in the optical system.[6] In this regard, many image edge detection approaches based on optical computing have been demonstrated, such as conventional phase contrast imaging,[7–10] the photonics spin Hall effect,[11] the Goos–Hänchen effect,[12] the Brewster effect[13] and other novel methods,[4] which are state-of-the-art technologies and most of which are utilized to achieve typical isotropic edge enhancement. Therefore, these approaches are not perfectly suited to some imaging cases where some directions with weak edges need to be preferentially emphasized more than other directions.

With further research on radial unsymmetric Hilbert transform filtering, two represented anisotropic edge detection methods, fractional vortex beam[14,15] and shifted vortex beam[16,17] approaches, have been demonstrated. Among them, the shifted vortex beam approach is conducted by interpreting the general radial Hilbert transform filtering as the format of a vortex and shifting the original position of singularity to break the symmetry of filtering.[16,17] In this way, the orientation of edge enhancement can be efficiently changed and can lead to strong anisotropic contrast imaging. Moreover, this unsymmetric Hilbert transform can immensely decline the data and procedures of imaging processing as it only extracts an image's important edge information and highlights the edges in need. However, to date, the function implementation of the anisotropic edge enhancement based on the above-mentioned methods is mainly by using a liquid crystal-based spatial light modulator, which provides dynamic phase or amplitude modulation for the optical input field by precision voltage regulation.[18] Therefore, it is not convenient enough compared with simple mode regulation of incident beams. Meanwhile, its bulky configuration and limited resolution hinder its applications in modern miniaturized and integrated systems.[16,19,20] Thus, building a simple, miniature, high-resolution, switchable anisotropic edge enhancement system is extremely absorbing.

Metasurfaces, composed of specifically designed subwavelength units in a two-dimensional plane, have become research hotspots due to their tremendous power in manipulating optical wavefronts.[21–25] They can replace several bulky traditional optical components to achieve various optical functions and allow light to be precisely regulated in the sub-wavelength thickness range. These potentials have pushed metasurfaces into different research areas, such as investigating the spin Hall effect,[26,27] tailoring multiple vortex beams,[28–30] metalenses[31,32]

[a] Beijing Key Laboratory for Precision Optoelectronic Measurement Instrument and Technology, School of Optics and Photonics, Beijing Institute of Technology, Beijing 100081, China. E-mail: huy08@bit.edu.cn
[b] College of Control Science and Engineering, China University of Petroleum, No. 66, West Changjiang Road, Qingdao, 266580, China

† Electronic supplementary information (ESI) available. See DOI: https://doi.org/10.1039/d3tc00092c

and metaholograms.[33–35] Meanwhile, a variety of functional imaging techniques based on metasurfaces,[36,37] like polarization imaging,[38,39] spectral imaging,[40,41] and isotropic edge detection,[18,27,42–44] are all attractive. To our best knowledge, current 2D switchable anisotropic edge-enhancement imaging *via* a metasurface also requires an external liquid-crystal plate based on additional voltage modulation.[45] Fortunately, the development of helicity-multiplexing metasurfaces brings great hope for this research.[46–49]

Here, a helicity-multiplexing metasurface (2D material) is designed based on the propagation phase and the geometry phase, which can dynamically switch between two various anisotropic edge enhancement filters only by transforming the polarization of the incident beam. This metasurface is composed of many nanopillars, which are all prioritized to be appropriate for two independent phase profiles. By embedding the metasurface into the focal plane of a Fourier transform in an optical system, we will demonstrate that this merging meta-4f imaging device enables the input field to achieve switchable 2D-anisotropic edge enhancement efficiently. The broadband characteristics will also be verified.

Principle and design

The overall design of the meta-4f system

Fig. 1 is the schematic of our meta-4f system setup, consisting of two traditional lenses and a helicity-multiplexing dielectric metasurface capable of dynamically switching between two different anisotropic edge enhancement imaging filters by changing the polarization of the incident beam. For example, as shown in Fig. 1(a), when the input object is the abbreviation "BIT", and the polarization of the incident beam is left-handed circular polarized (LCP), the output image is a left-enhanced anisotropic edge image of the object. Similarly, when this input object is under the illumination of a right-handed circular polarized (RCP) incident beam, the output information presented is a right-enhanced anisotropic edge image of the object, as shown in Fig. 1(b). The curvilinear figures in Fig. 1(a) and (b), respectively, show the corresponding cross-sectional intensity distributions at the white dashed line of the image in Fig. 1(a) and (b). We can observe the edge enhancement's anisotropic characteristics (left or right enhancement) from these. Other anisotropic edge enhancements can also be tailored, which will be shown later.

Principle of the meta-4f system

To illustrate the feasibility of our meta-4f system, we analyze the whole optical image processing of this system and the relevant principle in detail. In this system, the object can be seen as an electric field pattern of the LCP or RCP incident beam written as $E_{in}(x, y)$, where x and y are respectively, the x or y-direction coordinates in the input or output image plane. Then, a spatial Fourier transformation is performed by lens1 in Fig. 1(a). Our designed helicity-multiplexing dielectric metasurface functions as a dynamic spatial filter. Its optical spectrum

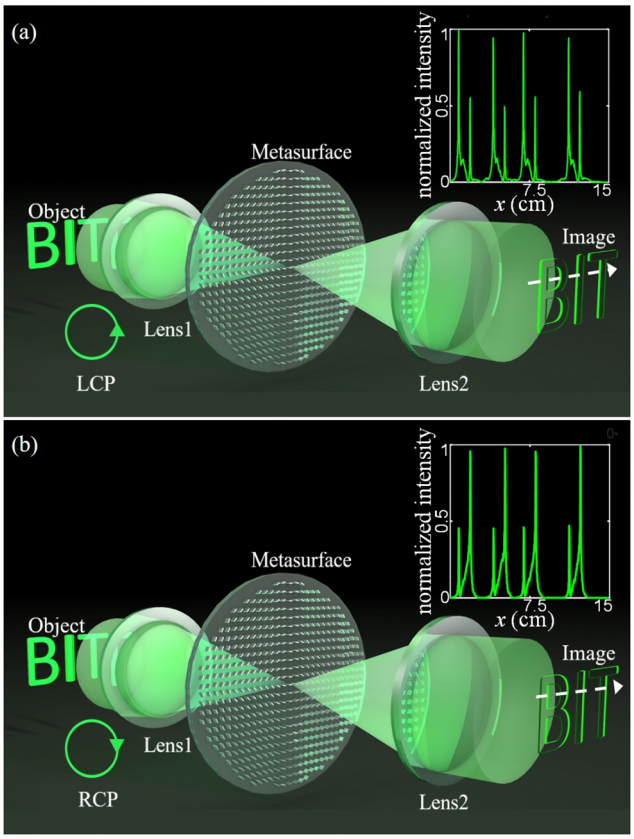

Fig. 1 Schematic of our meta-4f system setup. (a) A left-enhanced anisotropic edge image of the object "BIT" is obtained when illuminated by an LCP incident beam. (b) A right-enhanced anisotropic edge image of the object "BIT" is obtained when illuminated by an RCP incident beam. The curvilinear figures in the insets both represent the corresponding cross-sectional intensity distribution at the white dashed line of the image.

transfer function can be written as $H(f_x, f_y)$, where f_x and f_y are spatial frequency coordinates in the Fourier plane. After being modulated by our special spatial filter, the tailored electric field pattern is manipulated by lens2 in Fig. 1(a), and an inverse spatial Fourier transformation is performed. Therefore, the whole optical image processing can be concluded as follows:

$$E_{out}(x, y) = \mathrm{IFT}\{H(f_x, f_y)\cdot \mathrm{FT}[E_{in}(x, y)]\} \quad (1)$$

where, FT represents the 2D spatial Fourier transformation, and IFT represents the 2D inverse spatial Fourier transformation.

Next, one of the design keys is finding a proper $H(f_x, f_y)$ to help us efficiently achieve anisotropic edge enhancement. As mentioned above, a classical radial unsymmetric Hilbert transform[16] based on a complex amplitude modulation has been mathematically demonstrated. It breaks down the symmetry of the Hilbert transform by shifting the original position of singularity, and its phase modulation is dominant. Inspired by this, we infer that we can add an external phase distribution to the general spiral phase distribution corresponding to the classical radial symmetric Hilbert transform. Then we can easily change the singularity position only based on phase modulation. To protect the entire spiral phase filtering properties, we

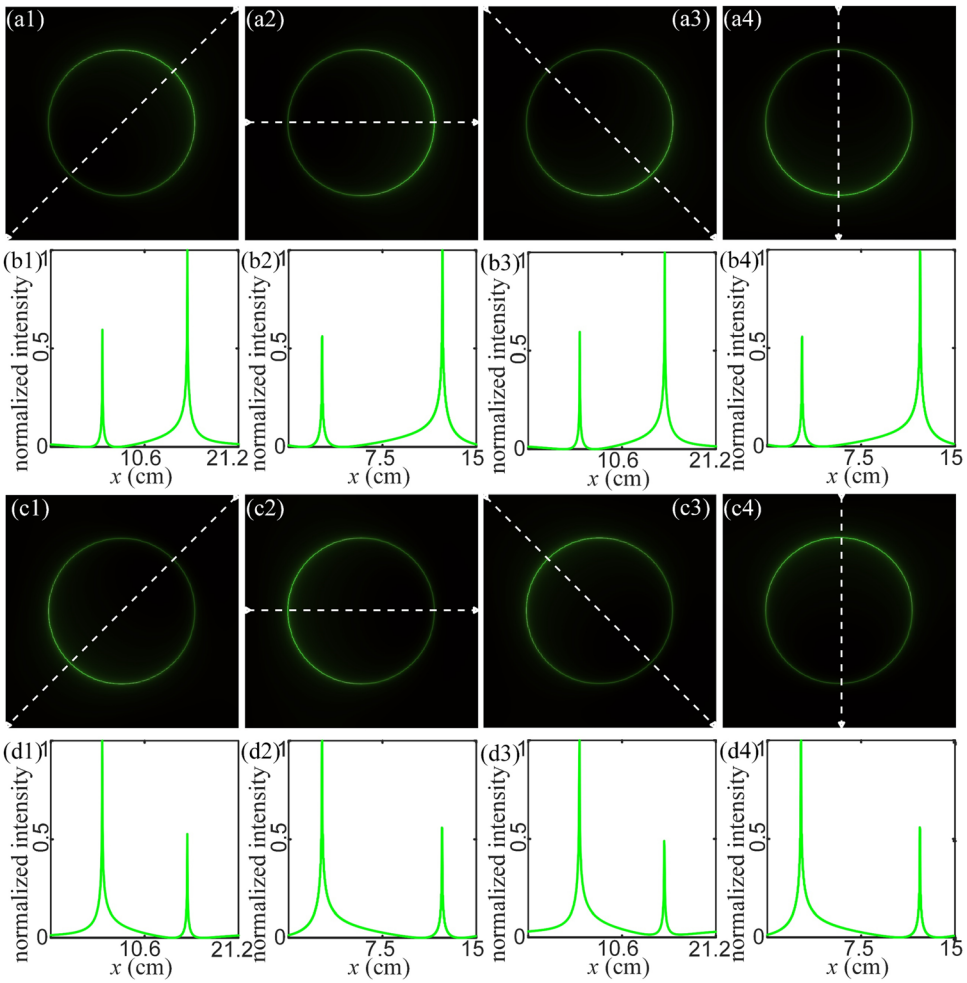

Fig. 2 Demonstration of the theoretical output results corresponding to the designed $H(f_x, f_y)$ when a circular pattern is the input object. (a1)–(a4) Theoretical output results as we set θ as $\pi/4$, $\pi/2$, $3\pi/4$, π, respectively. (b1)–(b4) Cross-sectional intensity curves of (a1)–(a4) along the white dashed lines. (c1)–(c4) Theoretical output results as we set θ as $5\pi/4$, $3\pi/2$, $7\pi/4$, and 2π, respectively. (d1)–(d4) Cross-sectional intensity curves of (c1)–(c4) along the white dashed lines.

utilize relevant coefficients like ρ_0 to control the additional phase effect. So, our $H(f_x, f_y)$ can be expressed as:

$$H(f_x, f_y) = \exp\left\{\mathrm{i} \cdot \mathrm{angle}\left[\frac{\rho \exp(i\phi) + \rho_0 \exp(\mathrm{i}\theta)}{\rho_1}\right]\right\}, \quad (2)$$

where, $f_x = u/(\lambda f)$, $f_y = v/(\lambda f)$, u and v are respectively the x or y-direction coordinates in the Fourier plane. Angle $(\cdot)$ represents the operation of extracting the phase of the expression in parentheses. $\rho^2 = u^2 + v^2$, $\phi = \arctan(v/u)$, and ρ_0 and θ are both real numbers. ${\rho_1}^2 = \rho^2 + {\rho_0}^2 + 2\rho_0\rho\cos(\phi - \theta)$. Normally, ρ_0 is less than the maximum of $\rho^{1/2}$. This way, several representative direction anisotropic edge enhancements can be efficiently achieved by changing the value of θ.

To observe this characteristic clearly, we keep $\rho_0 = 0.15\ \max(\rho^{1/2})$, choose different values of θ, and then gain several different distributions about $H(f_x, f_y)$. Here, a circular pattern is used as the object $E_{\mathrm{in}}(x, y)$. We can calculate the corresponding output field patterns $E_{\mathrm{out}}(x, y)$ with the help of the MATLAB platform, as shown in Fig. 2. Fig. 2(a1)–(a4) displays the output field distributions when $\theta = \pi/4$, $\pi/2$, $3\pi/4$ and π. The corresponding cross-sectional intensity curves are shown in Fig. 2(b1)–(b4). Subsequently, when we use $\theta = 5\pi/4$, $3\pi/2$, $7\pi/4$, and 2π, the obtained output field patterns and the corresponding cross-sectional intensity curves are respectively exhibited in Fig. 2(c1)–(c4) and (d1)–(d4). It can be found that there were various anisotropic edge enhancements along different directions when we changed the value of θ. In addition, we also observe the obtained theoretical results when different values of ρ_0 are chosen, and θ is set as π. From Fig. S1 (ESI†), different values of ρ_0 can affect the contrast of the anisotropic edge enhancement (see Note 1 of ESI†).

Therefore, the required phase profiles for our helicity-multiplexing metasurface mentioned in Fig. 1 can be written like this:

$$\psi_1 = \mathrm{angle}\left[\frac{\rho \exp(\mathrm{i}\phi) + \rho_0 \exp(\mathrm{i}3\pi/2)}{\rho_1}\right], \quad (3)$$

$$\psi_2 = \text{angle}\left[\frac{\rho \exp(i\phi) + \rho_0 \exp(i\pi/2)}{\rho_1}\right], \quad (4)$$

where, ψ_1 and ψ_2 are respectively the required phase profiles when the polarization of the incident beam is LCP or RCP. The corresponding phase maps are shown in Fig. S2 (ESI†).

Then, we divide the total phase of our metasurface into the propagation phase and the geometry phase, which can be respectively expressed[18] with the phase profiles in eqn (3) and (4) as:

$$\delta_x(x, y) = [\psi_1(x, y) + \psi_2(x, y)]/2 \quad (5)$$

$$\delta_y(x, y) = [\psi_1(x, y) + \psi_2(x, y)]/2 - \pi \quad (6)$$

$$2\vartheta(x, y) = [\psi_1(x, y) - \psi_2(x, y)]/2 \quad (7)$$

where, δ_x and δ_y are the propagation phase distributions for a linear polarization incident beam in the x- and y-directions, respectively, and 2ϑ is the geometric phase distribution.

Design of the metasurface

Fig. 3(a) and (b) respectively show the side and vertical views of a specifically designed unit cell to conform to the required propagation and geometric phases. It is a simple titanium dioxide nanopillar fabricated on a glass substrate. These nanopillars are periodically distributed with a fixed square lattice constant $P_x = P_y = 360$ nm and a height $H = 600$ nm. By changing the nanopillar's length L, and width W, we can construct the whole propagation phase library for choosing proper δ_x and δ_y that satisfy the relationships in eqn (5) and (6). The simulated phase δ_x for a linear polarization incident beam in the x-direction (XLP) as a function of L and W is shown in Fig. 3(c), and the corresponding transmission coefficient distribution t_x is displayed in Fig. 3(d). Homoplastically, the simulated phase δ_y and the corresponding transmission coefficient distribution t_y for a linear polarization incident beam in the y-direction (YLP) are respectively exhibited in Fig. 3(e) and (f). Considering the geometric phase, its control mechanism is by rotating the rotation orientation angle ϑ of the nanopillars, and it is twice the rotation orientation angle ϑ so that it can easily cover the entire phase library. In addition, all nanopillars are constructed to work as half-wave plates to maximize their polarization conversion efficiency. Underlying the above mechanism, we can obtain any ideal phase combination (δ_x, δ_y, and 2ϑ) by picking up an appropriate size and a rotation orientation angle (L, W, and ϑ) of the nanopillar. In this way, we can design our helicity-multiplexing metasurface to meet the phase profiles in eqn (3) and (4). The working wavelength of the incident laser is 532 nm. The simulation results are calculated through the commercial software, FDTD- solutions, where perfectly matching layers are used in the x, y, and z directions, and plane-wave sources are utilized.

Results

Fig. 4(a) and (b) respectively show the far-field phase distributions of the vortex beam generated by our metasurface (metasurface 1) when illuminated by an LCP or RCP incident beam. The spiral phase distributions in these two subfigures are different. Still, the corresponding intensity patterns in the center of the far-field intensity distributions are approximately equal (Fig. 4(c) and (d)). It means that our anisotropic edge enhancements are mainly manipulated by the pure phase, demonstrating the modulation mechanism that we mentioned in the section "Principle and design". Additionally, we also calculated

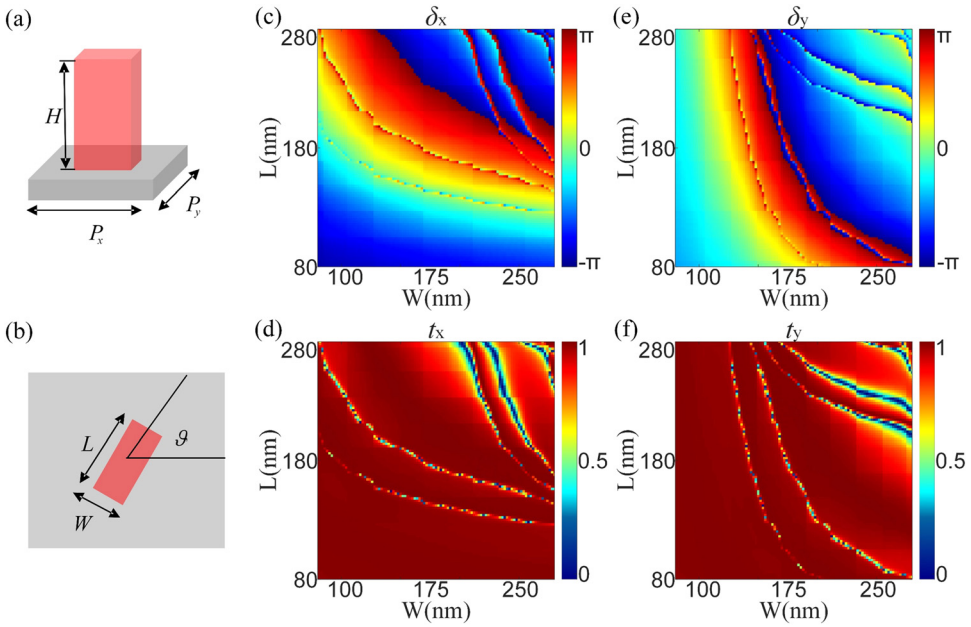

Fig. 3 (a) Side and (b) vertical view of a typical unit cell of the helicity-multiplexing metasurface with the period (P_x, P_y), height (H), varying cross section sizes (L and W), and different orientation rotation angles (ϑ). (c) Simulated propagation phase δ_x and (d) transmission coefficient t_x distributions for an XLP incident beam. (e) Simulated propagation phase δ_y and (f) transmission coefficient t_y distributions for a YLP incident beam.

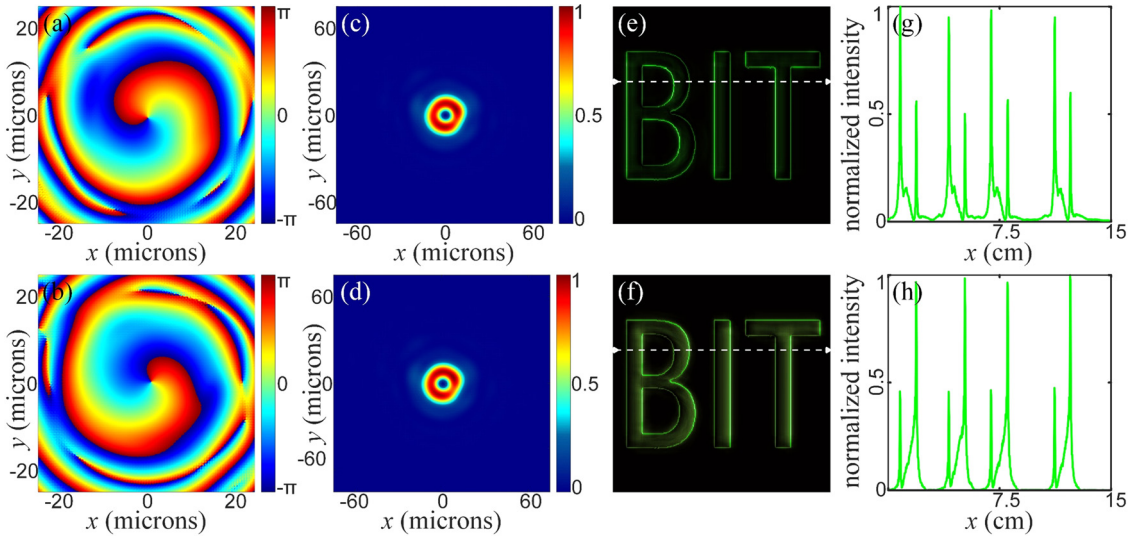

Fig. 4 (a) Simulated far-field phase distribution of metasurface 1 under the illumination of an LCP incident beam and (b) simulated far-field phase distribution of metasurface 1 under the illumination of an RCP incident beam; (c) and (d) depict the corresponding intensity patterns in the center of the far-field intensity distributions. (e) Output RCP field intensity distribution with a left enhanced edge of our meta-4f system under the illumination of an LCP incident beam and (f) output LCP field intensity distribution with a right enhanced edge of our meta-4f system under the illumination of an RCP incident beam. (g) and (h) Cross-sectional intensity distributions at the white dashed line position in (e) and (f), respectively.

the generated near-field phase profiles. The phase patterns maintain the spiral characteristic, and they are basically similar to our designed phase maps in eqn (3) and (4) (see Note 2 of ESI†). To evaluate the feasibility of our approach comprehensively, we also simulated the whole process. Fig. 4(e) and (f) are intensity distributions of the output field of the meta-4f system calculated by eqn (1), where the commercial software MATLAB is used to perform positive and inverse spatial Fourier transformations. When the polarization of the incident beam is LCP, the output RCP field intensity distribution is a left-enhanced anisotropic edge image of the abbreviation "BIT" as shown in Fig. 4(e). Similarly, when illuminated by the RCP incident beam, the output LCP field intensity pattern is a right-enhanced anisotropic edge image of "BIT," as shown in Fig. 4(f). Fig. 4(g) and (h) are respectively cross-sectional intensity distributions at the white dashed line position in Fig. 4(e) and (f), from which we can see the anisotropic edge enhancements

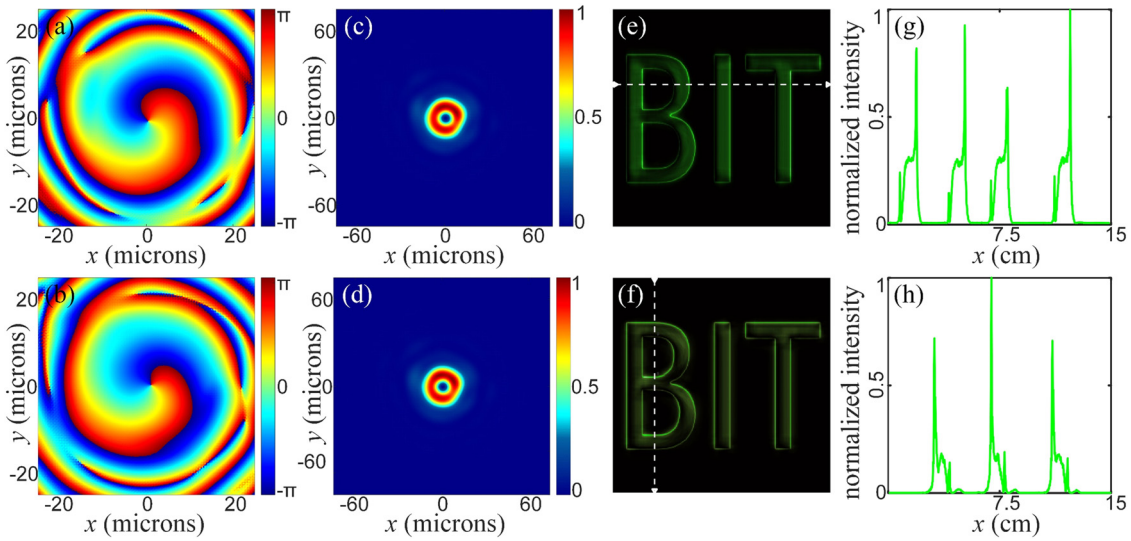

Fig. 5 (a) Simulated far-field phase distribution of metasurface 2 under the illumination of an LCP incident beam and (b) simulated far-field phase distribution of metasurface 2 under the illumination of an RCP incident beam; (c) and (d) depict the corresponding intensity patterns in the center of the far-field intensity distributions. (e) Output RCP field intensity distribution with a right enhanced edge of our meta-4f system under the illumination of an LCP incident beam and (f) output LCP field intensity distribution with a top enhanced edge of our meta-4f system under the illumination of an RCP incident beam. (g) and (h) Cross-sectional intensity distributions at the white dashed line position in (e) and (f), respectively.

in different directions more clearly. Therefore, this meta-4f system can achieve dynamic anisotropic edge enhancements by changing the polarization of the incident beam.

Furthermore, to verify our method's viability in achieving switchable anisotropic edge enhancements along other directions, we designed another metasurface (metasurface 2), which aims to achieve anisotropic edge enhancements along both horizontal and vertical directions. Therefore, the required phase profiles can be deduced like this:

$$\psi_1 = \text{angle}[(\rho \exp(i\phi) + (\rho_0 \exp(i\pi/2))/\rho_1] \quad (8)$$

$$\psi_2 = \text{angle}[(\rho \exp(i\phi) + (\rho_0 \exp(i2\pi))/\rho_1] \quad (9)$$

ψ_1 and ψ_2 are respectively shown in Fig. S2 (ESI†). The corresponding near-field phase distributions generated by metasurface 2 are also shown in Fig. S2 (ESI†), the spiral characteristics of which are well-maintained and generally similar to the phase maps in eqn (8) and (9) (see Note 2 of ESI†). The other simulated results are shown in Fig. 5. Fig. 5(a) and (b) respectively show the far-field phase patterns of the vortex beam generated by our metasurface under the illumination of an LCP or RCP incident beam. The spiral phase distributions in these two subfigures are also diverse, contributing to different anisotropic edge enhancements. Fig. 5(c) and (d) depict the corresponding intensity patterns in the center of the far-field intensity distributions, which are approximately equal. In addition, simulations of the whole process are also performed. Fig. 5(e) and (f) are output field patterns of the meta-4f system calculated by using eqn (1). The output RCP field intensity pattern is a right-enhanced anisotropic edge image of "BIT" under the illumination of an LCP incident beam, as shown in Fig. 5(e). When illuminated by the RCP incident beam, the output LCP field intensity pattern is a top-enhanced anisotropic edge image of "BIT," as shown in Fig. 5(f). Fig. 5(g) and (h) are respectively cross-sectional intensity distributions at the white dashed line position in Fig. 5(e) and (f). Thus, our approach can be utilized to design different metasurfaces for realizing various switchable anisotropic edge-enhanced imaging.

Since the geometry phase can work in a wide wavelength span, we infer that our designed helicity-multiplexing metasurfaces based on the propagation phase and the geometry phase can also work across broadband. To demonstrate the broadband functionalities of our meta-4f imaging system, another object, "M&I", the abbreviation for our laboratory, is used as an imaging target and is illuminated by beams of different wavelengths of 480 nm, 532 nm, and 630 nm. Metasurface 1 is

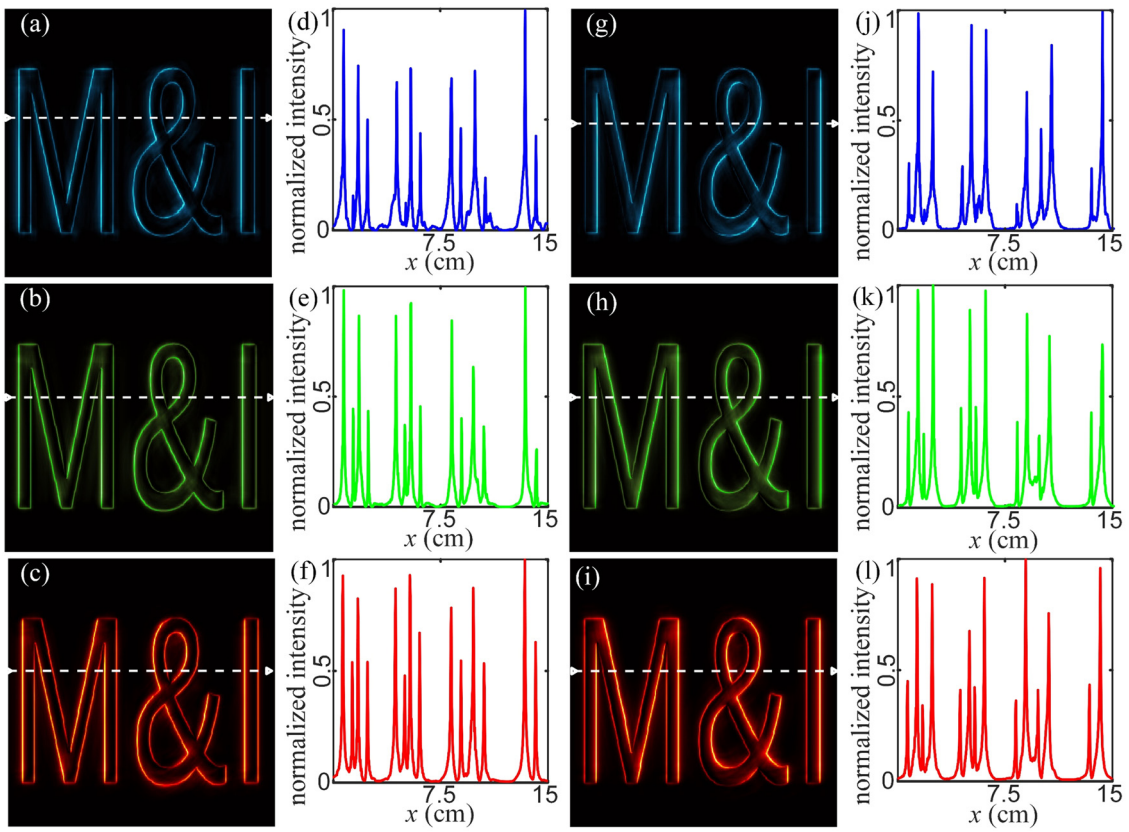

Fig. 6 (a)–(c) Output RCP field information of our meta-4f system under the illumination of an LCP incident beam at wavelengths of 480 nm, 532 nm, and 630 nm, respectively. (d)–(f) Field intensity distributions at the white dashed line position in (a)–(c), respectively. (g)–(i) Output LCP field information of our meta-4f system under the illumination of an RCP incident beam at wavelengths of 480 nm, 532 nm, and 630 nm. (j)–(l) Field intensity distributions at the white dashed line position in (g)–(i), respectively.

picked out as the spatial filter in the Fourier plane. The near-field phase patterns of the vortex beam generated by metasurface 1 under the illumination of 480 and 630 nm incident beams are shown respectively in Fig. S3 (ESI†). It is obvious that the spiral characteristics of the near-field distributions under the illumination of 480 nm are well-maintained, and their phase patterns are similar to those under the illumination of 532 nm. These absolute values of the near-field distributions at the wavelength of 630 nm are not similar enough to the results at the wavelength of 532 nm. Still, the spiral characteristics are well-maintained, *i.e.*, they are similar to those under the illumination of 532 nm, which is the key point at work. Fig. 6(a)–(c) show respectively the output RCP field intensity information of our meta-4f system under the illumination of LCP incident beams at wavelengths of 480 nm, 532 nm, and 630 nm. Fig. 6(d)–(f) show respectively the cross-sectional intensity distributions at the white dashed line positions in Fig. 6(a)–(c), from which it is obvious that left-enhancement anisotropic edge images can all be extracted. Similarly, Fig. 6(g)–(i) show respectively the output LCP field information of our meta-4f system under the illumination of RCP incident beams at a wavelengths of 480 nm, 532 nm, and 630 nm. Fig. 6(j)–(l) show respectively the cross-sectional intensity distributions at the white dashed line positions in Fig. 6(g)–(i), from which it is obvious that the right-enhancement anisotropic edge images can all be extracted. Therefore, our designed meta-4f system is not restricted to a specific wavelength and has a working bandwidth of at least 150 nm.

Conclusion

In conclusion, we have proposed and demonstrated a relevant 2D material, *i.e.*, two dielectric helicity-multiplexing metasurfaces, based on our proposed method. These metasurfaces can dynamically switch between two different functions (*i.e.*, generating different vortex beams) by altering two different polarizations of the incident beam, which correspond to two unrelated phase profiles. By endowing these metasurfaces with two different phase profiles and merging them into the 4f imaging system, we have demonstrated that this meta-4f imaging device can achieve two anisotropic edge enhancements along specific directions, including left and right or right and top. Furthermore, the broadband characteristics of our imaging device have been verified. Combined with the advantages of planar architecture and dynamically switchable functionalities across a broadband of the metasurface, we can envision that this meta-4f imaging device based on a designed 2D material holds potential applications in biomedical imaging and optical analog computing.

Author contributions

Qun Hao: supervised the overall study; Wenli Wang: performed the calculations and numerical analyses and finished the manuscript; Yao Hu: designed the simulations and finished the manuscript revisions; Jing Wang: finished the discussion of the frame of the manuscript and participated in the numerical analyses; Qianhui Li and Shaohui Zhang: participated in the manuscript revisions; Liandong Yu: participated in designing the frame of the manuscript.

Conflicts of interest

There are no conflicts to declare.

Acknowledgements

This work was supported by the National Natural Science Foundation of China (Grant No. 51735002, 62275022).

References

1 S. T. Acton and K. Ley, *in IEEE International Conference on Image Processing*, 2001, vol. 2, pp. 300–303.
2 A. H. Hernandez, D. G. Gill, P. R. Radeva and E. N. Nofrerias, in Computers in Cardiology, 2004, IEEE, pp. 229–232.
3 S. Hai-jiang, W. Yan-jie and C. Xiao-lin, *Opt. Precis. Eng*, 2014, **22**, 146–151.
4 H. Kwon, D. Sounas, A. Cordaro, A. Polman and A. Alù, *Phys. Rev. Lett.*, 2018, **121**, 173004.
5 T. J. Davis, F. Eftekhari, D. E. Gómez and A. Roberts, *Phys. Rev. Lett.*, 2019, **123**, 013901.
6 D. R. Solli and B. Jalali, *Nat. Photonics*, 2015, **9**, 704–706.
7 F. Zernike and F. J. M. Stratton, *Mon. Not. R. Astron. Soc.*, 1934, **94**, 377–384.
8 J. G. Dodd, *Appl. Opt.*, 1977, **16**, 470–472.
9 S. N. Khonina, V. V. Kotlyar, M. V. Shinkaryev, V. A. Soifer and G. V. Uspleniev, *J. Mod. Opt.*, 1992, **39**, 1147–1154.
10 J. A. Davis, D. E. McNamara, D. M. Cottrell and J. Campos, *Opt. Lett.*, 2000, **25**, 99–101.
11 S. He, J. Zhou, S. Chen, W. Shu, H. Luo and S. Wen, *APL Photonics*, 2020, **5**, 036105.
12 D. Xu, S. He, J. Zhou, S. Chen, S. Wen and H. Luo, *Appl. Phys. Lett.*, 2020, **116**, 211103.
13 T. Zhu, C. Guo, J. Huang, H. Wang, M. Orenstein, Z. Ruan and S. Fan, *Nat. Commun.*, 2021, **12**, 680.
14 A. W. Lohmann, D. Mendlovic and Z. Zalevsky, *Opt. Lett.*, 1996, **21**, 281–283.
15 J. Wang, W. Zhang, Q. Qi, S. Zheng and L. Chen, *Sci. Rep.*, 2015, **5**, 15826.
16 G. Situ, G. Pedrini and W. Osten, *J. Opt. Soc. Am. A*, 2009, **26**, 1788–1797.
17 M. K. Sharma, J. Joseph and P. Senthilkumaran, *J. Opt.*, 2013, **42**, 1–7.
18 P. Huo, C. Zhang, W. Zhu, M. Liu, S. Zhang, S. Zhang, L. Chen, H. J. Lezec, A. Agrawal, Y. Lu and T. Xu, *Nano Lett.*, 2020, **20**, 2791–2798.
19 A. Jesacher, S. Fürhapter, S. Bernet and M. Ritsch-Marte, *Phys. Rev. Lett.*, 2005, **94**, 233902.

20 C. Maurer, A. Jesacher, S. Bernet and M. Ritsch-Marte, *Laser Photon. Rev.*, 2011, **5**, 81–101.
21 D. Lin, P. Fan, E. Hasman and M. L. Brongersma, *Science*, 2014, **345**, 298–302.
22 S. Kruk and Y. Kivshar, *ACS Photonics*, 2017, **4**, 2638–2649.
23 S. Divitt, W. Zhu, C. Zhang, H. J. Lezec and A. Agrawal, *Science*, 2019, **364**, 890–894.
24 M. Pan, Y. Fu, M. Zheng, H. Chen, Y. Zang, H. Duan, Q. Li, M. Qiu and Y. Hu, *Light: Sci. Appl.*, 2022, **11**, 195.
25 H. Jeong, Y. Yang, H. Cho, T. Badloe, I. Kim, R.-M. Ma and J. Rho, *Microelectron. Eng.*, 2020, **220**, 111146.
26 X. Yin, Z. Ye, J. Rho, Y. Wang and X. Zhang, *Science*, 2013, **339**, 1405–1407.
27 J. Zhou, H. Qian, C.-F. Chen, J. Zhao, G. Li, Q. Wu, H. Luo, S. Wen and Z. Liu, *Proc. Natl. Acad. Sci. U. S. A.*, 2019, **116**, 11137–11140.
28 Y. Bao, J. Ni and C. Qiu, *Adv. Mater.*, 2020, **32**, 1905659.
29 H. Yang, Z. Xie, G. Li, K. Ou, F. Yu, H. He, H. Wang and X. Yuan, *Photonics Res.*, 2021, **9**, 331–343.
30 Q. Hao, W. Wang, Y. Hu, S. Zhang, S. Zhang and Y. Zhang, *Opt. Mater. Express*, 2022, **12**, 3872–3881.
31 M. Khorasaninejad, W. T. Chen, R. C. Devlin, J. Oh, A. Y. Zhu and F. Capasso, *Science*, 2016, **352**, 1190–1194.
32 K. Ou, F. Yu, G. Li, W. Wang, A. E. Miroshnichenko, L. Huang, P. Wang, T. Li, Z. Li, X. Chen and W. Lu, *Sci. Adv.*, 2020, **6**, eabc0711.
33 X. Fang, H. Ren and M. Gu, *Nat. Photonics*, 2020, **14**, 102–108.
34 X. Li, X. Zhang, R. Zhao, G. Geng, J. Li, L. Huang and Y. Wang, *Laser Photon. Rev.*, 2022, **16**, 2100592.
35 J. Burch, J. Ma, R. I. Hunter, S. A. Schulz, D. A. Robertson, G. M. Smith, J. Wang and A. D. I. Falco, *Appl. Phys. Lett.*, 2019, **115**, 021104.
36 K. Cheng, Z. Li, J. Wu, Z.-D. Hu and J. Wang, *Opt. Express*, 2022, **30**, 2780–2791.
37 M. Li, M. Liu, Y. Chen, Z. Da Hu, J. Wu and J. Wang, *Nanoscale Res. Lett.*, 2022, **17**, 81.
38 N. A. Rubin, G. D'Aversa, P. Chevalier, Z. Shi, W. T. Chen and F. Capasso, *Science*, 2019, **365**, eaax1839.
39 Y. Hu, X. Wang, X. Luo, X. Ou, L. Li, Y. Chen, P. Yang, S. Wang and H. Duan, *Nanophotonics*, 2020, **9**, 3755–3780.
40 A. McClung, S. Samudrala, M. Torfeh, M. Mansouree and A. Arbabi, *Sci. Adv.*, 2020, **6**, eabc7646.
41 X. Hua, Y. Wang, S. Wang, X. Zou, Y. Zhou, L. Li, F. Yan, X. Cao, S. Xiao, D. P. Tsai, J. Han, Z. Wang and S. Zhu, *Nat. Commun.*, 2022, **13**, 2732.
42 H. Yang, Z. Xie, H. He, Q. Zhang, J. Li, Y. Zhang and X. Yuan, *Opt. Lett.*, 2021, **46**, 3741–3744.
43 Z. Wang, G. Hu, X. Wang, X. Ding, K. Zhang, H. Li, S. N. Burokur, Q. Wu, J. Liu, J. Tan and C.-W. Qiu, *Nat. Commun.*, 2022, **13**, 2188.
44 T. Badloe, S. Lee and J. Rho, *Adv. Photonics*, 2022, **4**, 064002.
45 T. Xiao, H. Yang, Q. Yang, D. Xu, R. Wang, S. Chen and H. Luo, *Opt. Lett.*, 2022, **47**, 925–928.
46 T. Badloe, I. Kim, Y. Kim, J. Kim and J. Rho, *Adv. Sci.*, 2021, **8**, 2102646.
47 M. A. Naveed, M. A. Ansari, I. Kim, T. Badloe, J. Kim, D. K. Oh, K. Riaz, T. Tauqeer, U. Younis, M. Saleem, M. S. Anwar, M. Zubair, M. Q. Mehmood and J. Rho, *Microsyst. Nanoeng.*, 2021, **7**, 5.
48 H. S. Khaliq, I. Kim, J. Kim, D. K. Oh, M. Zubair, K. Riaz, M. Q. Mehmood and J. Rho, *Adv. Opt. Mater.*, 2021, **9**, 2002002.
49 Y. Yang, H. Kim, T. Badloe and J. Rho, *Nanophotonics*, 2022, **11**, 4123–4133.